

DIRECT SIMULATION OF HYBRID POWER-LAW LEADING EDGE IN HYPERSONIC FLOW

Wilson F. N. Santos

wilson@lcp.inpe.br

Combustion and Propulsion Laboratory
National Institute for Space Research
Cachoeira Paulista, SP 12630-000

The aerodynamic characteristics of a family of hybrid power-law leading edges immersed in high-speed rarefied flow are examined by using the Direct Simulation Monte Carlo (DSMC) method. The work is motivated by the fact that power-law leading edge shapes have characteristics of a sharp body (infinite body slope) and of a blunt body (zero radius of curvature) at the nose. The aerodynamic surface quantities for hybrid power-law shapes are compared to those for symmetric power-law shapes. The results presented highlight the sensitivity of the heat transfer coefficient, pressure coefficient, skin friction coefficient, total drag and total lift due to changes on the power-law exponent of the upper surface shape of the leading edges. Interesting features for sharp and blunt leading edges were noted on the computational results for the aerodynamic surface quantities. It was found that the stagnation point heating for hybrid power-law leading edges are smaller than that for symmetric power-law leading edges. The analysis also indicated that the total drag for the symmetric power-law leading edges is smaller than that for hybrid power-law leading edges under the range of conditions investigated.

Keywords: DSMC, Hypersonic flow, Rarefied flow, Power-Law Shape, Aerodynamic Heating.

1. INTRODUCTION

At hypersonic flight speeds, the vehicle leading edges should be blunt to some extent in order to reduce the heat transfer rate to acceptable levels and to allow for internal heat conduction. The use of blunt-nose shapes tends to alleviate the aerodynamic heating problem since the heat flux for blunt bodies is far lower than that for sharply pointed bodies. In addition, the reduction in heating rate for a blunt body is accompanied by an increase in heat capacity, due to the increased volume. Due mainly to manufacturing problems and the extremely high temperatures attained in hypersonic flight, hypersonic vehicles should have blunt nose, although probably slendering out at a short distance from the nose.

Usually, a round leading edge with constant radius of curvature (circular cylinder) near the stagnation point has been chosen for blunting geometry. Nevertheless, shock detachment distance on a cylinder scales with the radius of curvature. As a result, shock wave detachment will allow pressure leakage from the lower surface of the vehicle to the upper surface, thereby degrading the aerodynamic performance of vehicle such as waveriders (Nonweiler, 1959). Hypersonic waveriders depend on leading edge shock attachment to their forward surface in order to contain the high pressure air that produces useful lifting force. It is the shock attachment that produces de high lift-to-drag (L/D) ratio observed in waverider vehicles.

In this scenario, power-law shaped leading edges ($y \propto x^p$, $0 < p < 1$) may provide the required bluntness for heat transfer and manufacturing concerns with less increase in shock wave detachment so that the final design more closely approximates the ideal aerodynamic performance. This concept is based on work of Mason and Lee (1994) that pointed out, based on Newtonian flow analysis, that these shapes exhibit both blunt and sharp aerodynamic properties. According to them, for values of $0 < p < 1$, the slope of the power-law shape is infinite at $x = 0$, a characteristic of a blunt body. However, for $1/2 < p < 1$, the radius of curvature at the nose approaches zero, a characteristic of a sharp body.

A great deal of experimental and theoretical works has been carried out previously on power-law forms representing blunt geometries. Of particular interest are the works by Santos and Lewis (2002, 2005a, and 2005b) and by Santos (2005, and 2008). The major interest in these works has gone into considering the power-law shape as possible candidate for blunting geometries of hypersonic waverider leading edge.

Through the use of the Direct Simulation Monte Carlo (DSMC) method, Santos and Lewis (2002 and 2005b) found that the stagnation point heating behavior for power-law leading edges with finite radius of curvature, $p = 1/2$, followed that predicted for classical blunt body in that the heating rate is inversely proportional to the square root of curvature radius at the stagnation point. For those power-law leading edges with zero radii of curvature, $p > 1/2$, it was found that the stagnation point heating is not a function of the curvature radius at the vicinity of the leading edges, but agreed with the classical blunt body behavior predicted by the continuum flow far from the stagnation point. Results were compared to a corresponding circular cylinder to determine which geometry would be better suited as a blunting profile. Their analysis also showed that power-law shapes provided smaller total drag than the circular cylinder, typically used in blunting sharp leading edges for heat transfer considerations. However, circular cylinder provided smaller stagnation point heating than power-law shapes under the range of conditions investigated.

In order to assess the advantages and disadvantages of a power-law body, computational results are obtained for a different scenario of power-law shapes. In the present account, the aerodynamic surface quantities are investigated for hybrid power-law shapes, i.e., lower and upper surface with different power-law exponents.

In this connection, the purpose of this work is to examine computationally the shape effects on the heat flux to and on the drag of hybrid power-law leading edges in order to

provide information on how well these shapes stand up as possible candidates for blunting geometries of hypersonic leading edges. The aerodynamic surface quantities, heat flux and drag, will be investigated for a combination of power-law exponents of 1/2, 3/5, 2/3 and 3/4 for the upper and lower surface shapes.

2. LEADING-EDGE GEOMETRY

In dimensional form, the body power-law shapes are given by the following expression,

$$y = Ax^p \quad (1)$$

where p is the power-law exponent and A is the power-law constant which is a function of p .

In the previous work (Santos and Lewis, 2002), the power-law shapes were modeled by assuming a sharp-edged wedge of half angle θ with a circular cylinder of radius R inscribed tangent to this wedge. The power-law shapes, inscribed between the wedge and the cylinder, are also tangent to them at the same common point where they have the same slope angle. The circular cylinder diameter provides a reference for the amount of blunting desired on the leading edges. It was assumed a leading-edge half angle of 10 degrees, a circular cylinder diameter of 10^{-2} m and power-law exponents of 1/2, 3/5, 2/3, 7/10, 3/4, and 4/5. Figure 1(a) illustrates schematically this construction for the set of symmetric power-law leading edges previously investigated.

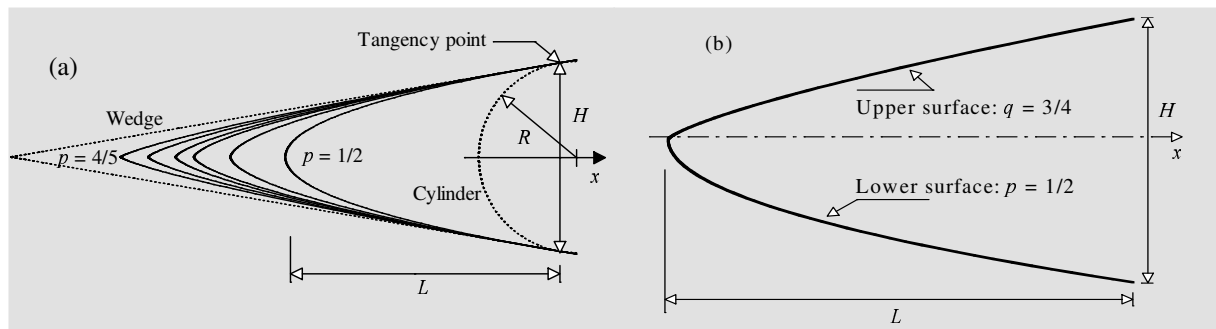


Figure 1: Drawing illustrating the (a) symmetric and (b) the hybrid power-law leading edges.

From geometric considerations, the common body height H , Figure 1(a), at the tangency point is equal to $2R\cos\theta$. The power-law constant A , obtained by matching slope on the wedge, circular cylinder and power-law body at the tangency point is given as follows,

$$A = \frac{\left(\frac{R^2}{1 + \tan^2 \theta} \right)^{(1-p)/2}}{\left(\frac{p}{\tan \theta} \right)^p} \quad (2)$$

As the slope of the power-law shapes is infinite at $x = 0$, i.e., the slope angle is 90 degrees, the hybrid power-law shapes were obtained by combining the upper and lower part of the curves, with respect to the symmetry line, shown in Figure 1(a). In this way, for the hybrid power-law shapes, the upper surface was represented by the exponent q of 3/5, 2/3 or 3/4 and the lower surface by the exponent p of 1/2. Figure 1(b) illustrates a hybrid power-law leading edge defined by $q = 3/4$ and $p = 1/2$.

It was assumed that the hybrid power-law leading edges are infinitely long but only the length L is considered in the simulation since the wake region behind the power-law bodies is not of interest in this investigation.

3. COMPUTATIONAL METHOD

The choice of the numerical approach to be used to model rarefied non-equilibrium flows greatly relies on the extent of flow rarefaction. For near-continuum flows, it is usually sufficient to take into account the effects of rarefaction through the boundary conditions of slip velocity and temperature jump on the surface. The Navier-Stokes equations, commonly used with these boundary conditions, can be derived from the transport Boltzmann equation under the assumption of small deviation of the distribution function from equilibrium. Nevertheless, the Navier-Stokes equations became unsuitable for studying rarefied flows where the distribution function becomes considerable in non-equilibrium.

In order to study rarefied flow with a significant degree of non-equilibrium, the Direct Simulation Monte Carlo (DSMC) method (Bird, 1994) is usually employed. The DSMC method has become the most common computational technique for modeling complex transitional flows of engineering interest.

The DSMC method model a gas flow by using a computer to track the trajectory of simulated particles, where each simulated particle represents a fixed number of real gas particles. The simulated particles are allowed to move and collide, while the computer stores their position coordinates, velocities and other physical properties such as internal energy. The simulation is always calculated as unsteady flow. However, a steady flow solution is obtained as the large time state of the simulation.

The molecular collisions are modeled by using the variable hard sphere (VHS) molecular model (Bird, 1981) and the no time counter (NTC) collision sampling technique (Bird, 1989). The energy exchange between kinetic and internal modes is controlled by the Borgnakke-Larsen statistical model (Borgnakke and Larsen, 1975). Simulations are performed using a non-reacting gas model consisting of two chemical species, N_2 and O_2 . Energy exchanges between the translational and internal modes, rotational and vibrational, are considered. For a given collision, the probabilities are designated by the inverse of the relaxation numbers, which correspond to the number of collisions necessary, on average, for a molecule to relax. Relaxation collision numbers of 5 and 50 were used for the calculations of rotation and vibration, respectively.

4. COMPUTATIONAL DOMAIN AND GRID

In order to implement the particle-particle collisions, the flowfield is divided into an arbitrary number of regions, which are subdivided into computational cells. The cells are further subdivided into four subcells, two subcells/cell in each direction. The cell provides a convenient reference sampling of the macroscopic gas properties, whereas the collision partners are selected from the same subcell for the establishment of the collision rate. As a result, the flow resolution is much higher than the cell resolution. The dimensions of the cells must be such that the change in flow properties across each cell is small. The linear dimensions of the cells should be small in comparison with the distance over which there is a significant change in the flow properties. These conditions define that the cell dimensions should be of the order of the local mean free path or even smaller (Alexander et al., 1998 and 2000).

The computational domain used for the calculation is made large enough so that body disturbances do not reach the upstream and side boundaries, where freestream conditions are

specified. A schematic view of the computational domain is depicted in Figure 2. Side I is defined by the body surface. Diffuse reflection with complete thermal accommodation is the condition applied to this side. Side II is the freestream side through which simulated molecules enter and exit. Finally, side III is the downstream outflow boundary. At this boundary, the flow is predominantly supersonic and vacuum condition is specified (Guo and Liaw, 2001). As a result, it is assumed that at this boundary simulated molecules can only exit.

The effects of grid resolution and the effects of the number of particles per computational cell were investigated in order to determine the number of cells and the number of particles required to achieve grid independence solutions. In this fashion, a grid independence study was made with three different structured meshes in each coordinate direction. The effect of altering the cell size in the ξ -direction was investigated with grids of 60(coarse), 90(standard) and 120(fine) cells on the upper and lower surfaces, and 60 cells in the η -direction for the leading edges investigated. In analogous manner, an examination was made in the η -direction with grids of 30(coarse), 60(standard) and 90(fine) cells, and 90 cells along the upper and lower surface, i.e., in the ξ -direction. In

addition, each grid was made up of non-uniform cell spacing in both directions. The effect (not shown) of changing the cell size in both directions on the heat transfer and pressure coefficients was rather insensitive to the range of cell spacing considered, indicating that the standard grid, 180x60 cells in the entire domain is essentially grid independent. A similar procedure was performed with respect to the number of particles. The total number of particles depends on the case investigated. On the average, it is around of 350,000 particles.

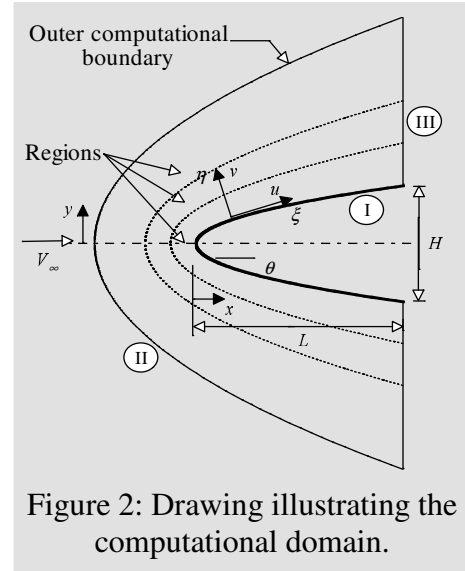


Figure 2: Drawing illustrating the computational domain.

5. COMPUTATIONAL CONDITIONS

DSMC simulations have been performed based on the flow conditions given by Santos and Lewis (2002) and summarized in Table 1, and the gas properties (Bird, 1994) are shown in Table 2.

Table 1. Freestream and flow conditions

Temperature T_∞ (K)	Pressure p_∞ (N/m ²)	Density ρ_∞ (kg/m ³)	Number density n_∞ (m ⁻³)	Viscosity μ_∞ (Ns/m ²)	Mean free path λ_∞ (m)
220.0	5.582	8.753×10^{-5}	1.8209×10^{21}	1.455×10^{-5}	9.03×10^{-4}

Table 2. Gas properties

	Mole fraction X	Molecular mass m (kg)	Molecular diameter d (m)	Viscosity index ω
O ₂	0.237	5.312×10^{-26}	4.01×10^{-10}	0.77
N ₂	0.763	4.650×10^{-26}	4.11×10^{-10}	0.74

The freestream velocity V_∞ is assumed to be constant at 3.56 km/s. This velocity corresponds to a freestream Mach number M_∞ of 12. The translational and vibrational

temperatures in the freestream are in equilibrium at 220 K. The wall temperature T_w is assumed constant at 880 K. This temperature is chosen to be representative of the surface temperature near the stagnation point and is assumed to be uniform over the entire leading edges.

The freestream Knudsen number Kn_∞ , defined as the ratio of the molecular mean free path λ in the freestream gas to a characteristic dimension of the flowfield, corresponds to 0.0903, where the characteristic dimension was defined as being the diameter of the reference circular cylinder (see Figure 1). The freestream Reynolds number Re_∞ by unit meter is 21,455.

In order to simulate the shape effects, the DSMC calculations were performed independently for a family of hybrid power-law leading edges. The upper surface shape, represented by the exponent q , assumed the values 1/2, 3/5, 2/3 and 3/4, and the lower surface shape, referred by the exponent p , was fixed at 1/2. It should be mentioned in this context that the leading edge defined by $p = q = 1/2$ represents the symmetric power-law leading edge investigated previously by Santos and Lewis (2002).

6. COMPUTATIONAL RESULTS AND DISCUSSION

This section focuses on the effects that take place in the aerodynamic surface quantities due to the variations on the leading-edge shape. Aerodynamic surface quantities of particular interest in the transition flow regime are number flux, heat transfer, pressure, skin friction, drag and lift. In this scenario, this section discusses and compares differences of these quantities, expressed in a coefficient form, for the leading edges investigated.

6.1 Number flux

The number flux N is calculated by sampling the molecules impinging on the surface by unit time and unit area. A flux is regarded as positive if it is directed toward the body surface. The dependence of the number flux on the leading-edge shape is illustrated in Figures 3(a) and 3(b) for the lower and upper surfaces, respectively. In this set of plots, the dimensionless number flux N_f stands for the number flux N normalized by $n_\infty V_\infty$, where n_∞ is the freestream number density and V_∞ is the freestream velocity. In addition, S is the arc length s along the body surface, measured from the stagnation point, normalized by the freestream mean free path λ_∞ . Also, p and q refer to the power-law exponents of the lower and upper surfaces, respectively. For comparison purpose, the symmetric case of $p = q = 1/2$ is shown in the plots.

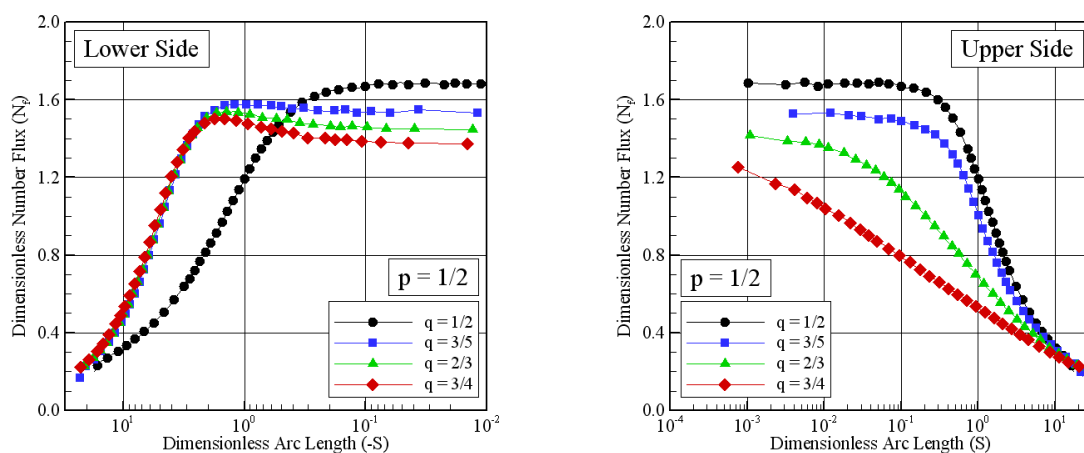


Figure 3: Distributions of the dimensionless number flux N_f along the (a) lower and (b) upper surfaces as a function of the arc length S and parameterized by the power-law exponents.

According to Figures 3(a) and 3(b), for the symmetric case of $p = q = 1/2$, it is noted that the number flux presents a constant high value at the vicinity of the stagnation region, then the number flux N_f drops off sharply along the body surface. As the power-law exponent q increases from $1/2$ to $3/4$, i.e., only the shape of the upper surface is changed, the number flux decreases along the upper surface and significantly increases along the lower surface. With increasing q , the upper surface becomes sharp as compared to the lower surface. As a result, due to the flow compression on the lower surface and the flow expansion on the upper surface of the leading edge, the pick value for the number flux moves from the stagnation point to a station on the lower surface.

At least at first sight, this behavior may be related to the collisions of two groups of molecules; the molecules reflecting from the nose of the leading edge and the molecules oncoming from the freestream. The molecules that are reflected from the lower body surface, which have a lower kinetic energy interact with the oncoming freestream molecules, which have a higher kinetic energy. Thus, the surface-reflected molecules re-collide with the body surface, which produce an increase in the dimensionless number flux in this region. Therefore, it is very encouraging to observe that the entire flowfield structure around the leading edge is altered by changing only the shape of the upper surface.

The leading-edge shape effect can also be seen in a different way by comparing the DSMC results with those calculated by assuming free molecular flow (Bird, 1994). Free-molecular flow or collisionless flow is the limiting case in which the Knudsen number tends to infinity. It is the subdivision of rarefied gas dynamics corresponding to the lowest densities, therefore with very high mean free paths, or with very small characteristic dimensions. Figure 4 presents this comparison for the dimensionless number flux N_f as a function of the body surface slope angle. These curves indicate that the number flux on the lower and upper surfaces is above that predicted by the free molecular flow. At the stagnation point, the free molecular flow equation predicts a dimensionless number flux $N_f = 1$. It means that $N/n_\infty V_\infty = 1$. Also of great significance is the pick value for the number flux. For the symmetric leading-edge shape, $p = q = 1/2$, it takes place at the stagnation point. Nevertheless, as the upper surface shape changes, by means of increasing q , the pick value moves to the lower side of the leading edges at stations that correspond to the body slope angles from 35 to 45 degrees.

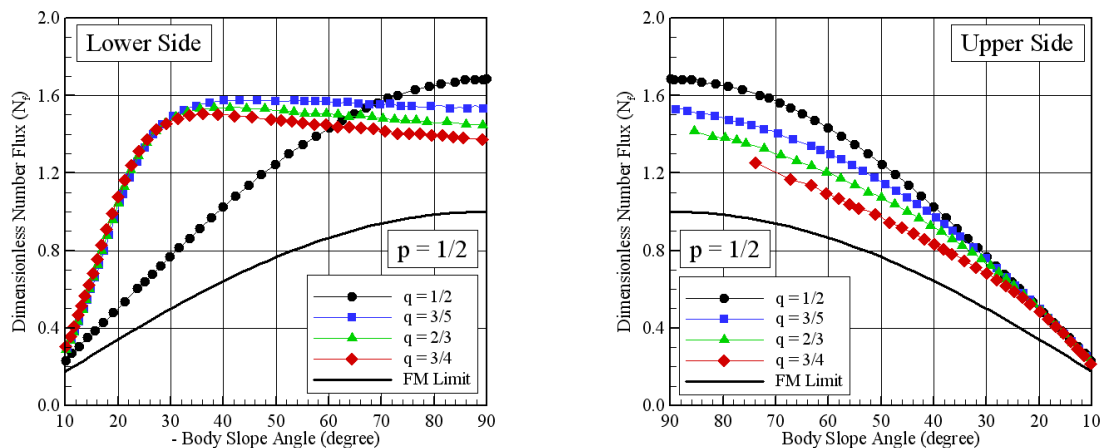


Figure 4: Distributions of the dimensionless number flux N_f along the (a) lower and (b) upper surfaces as a function of the body slope angle and parameterized by the power-law exponents.

6.2 Heat transfer coefficient

The heat transfer coefficient C_h is defined as being,

$$C_h = \frac{q_w}{\frac{1}{2}\rho_\infty V_\infty^3} \quad (3)$$

where q_w is the net heat flux to the body surface and ρ_∞ is the freestream density.

The heat flux q_w to the body surface is calculated by the net energy flux of the molecules impinging on the surface. The net heat flux q_w is related to the sum of the translational, rotational and vibrational energies of both incident and reflected molecules as defined by,

$$q_w = q_i + q_r = \sum_{j=1}^N \left\{ \left[\frac{1}{2} m_j v_j^2 + e_{Rj} + e_{Vj} \right]_i + \left[\frac{1}{2} m_j v_j^2 + e_{Rj} + e_{Vj} \right]_r \right\} \quad (4)$$

where N is the number of molecules colliding with the surface by unit time and unit area, m is the mass of the molecules, v is the velocity of the molecules, e_R and e_V stand for the rotational and vibrational energies, respectively. Subscripts i and r refer to incident and reflected molecules.

The impact of the leading-edge shape on the heat transfer coefficient C_h is illustrated in Figures 5(a) and 5(b) for lower and upper surfaces, respectively. It is clearly noticed from these plots that the heat transfer coefficient C_h is sensitive to changes on the upper surface shape. For the symmetric case of $p = q = 1/2$, the heat transfer coefficient C_h presents the maximum value at the stagnation region and drops off sharply downstream along the body surface. By increasing the power-law exponent q from $1/2$ to $3/4$, the expected asymmetry in the heat transfer coefficient distribution is observed, with the heat transfer coefficient C_h increasing on the stagnation region and along the lower surface.

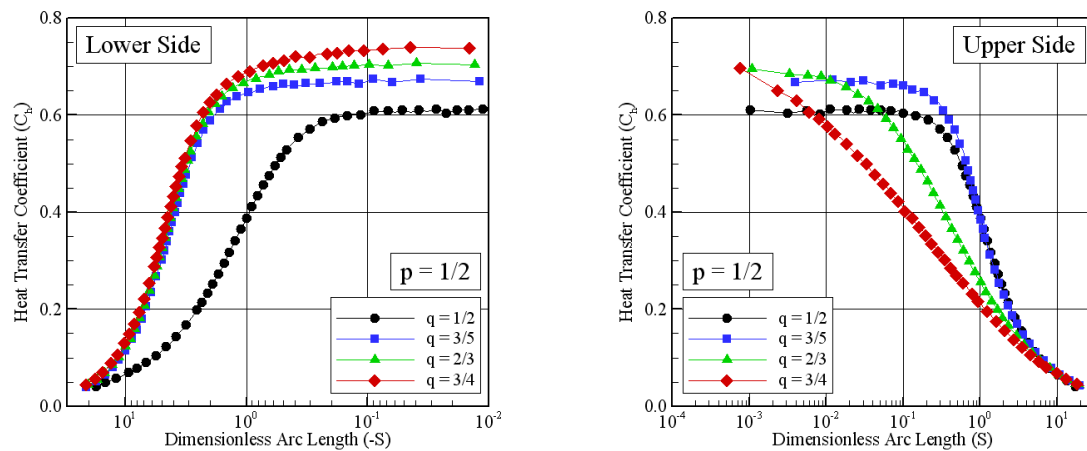


Figure 5: Distributions of the heat transfer coefficient C_h along the (a) lower and (b) upper surfaces as a function of the arc length S and parameterized by the power-law exponents.

Before proceeding with the analysis, it is desirable to present the heat transfer coefficient C_h as a function of the body slope angle. In this fashion, Figures 6(a) and 6(b) depict the heat transfer coefficient along the upper and lower surfaces, respectively. For comparison purpose, the heat transfer coefficient predicted by assuming free molecular flow is also depicted in this group of diagrams.

Referring to Figures 6(a) and 6(b), it is very encouraging to observe that the heat transfer coefficient presents the pick value at the stagnation point. In addition to that, the pick value increases with increasing the power-law exponent q from $1/2$ to $3/4$. It may be inferred in passing that the maximum heat transfer coefficient C_h attained at the stagnation point does not

correspond to the maximum number flux. The heat transfer coefficient at the stagnation point C_{ho} , obtained by a curve fitting process performed over the curves displayed in these figures, corresponds approximately to 0.605, 0.672, 0.703, and 0.739 for leading-edge shapes given by power-law exponent q of 1/2, 3/5, 2/3 and 3/4, respectively. As a base of comparison, the heat transfer coefficient at the stagnation point C_{ho} for symmetric power-law leading edges (Santos and Lewis, 2002) with exponents of 3/5, 2/3 and 3/4 is 0.730, 0.785 and 0.858, respectively. Consequently, it is firmly established that the hybrid power-law leading edges investigated present a smaller heat transfer coefficient at the stagnation point than their corresponding symmetric power-law leading edges.

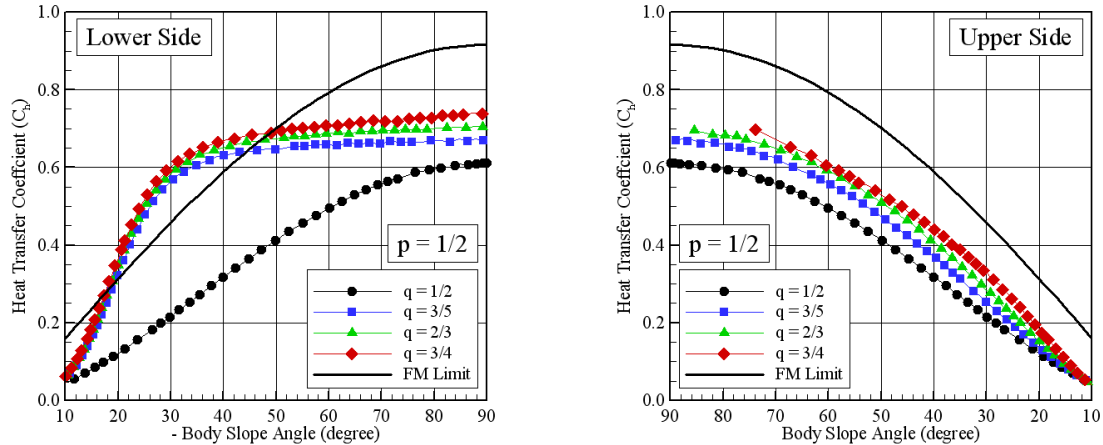


Figure 6: Distributions of the heat transfer coefficient C_h along the (a) lower and (b) upper surfaces as a function of the body slope angle and parameterized by the power-law exponents.

6.3 Pressure coefficient

The pressure coefficient C_p is defined as being,

$$C_p = \frac{p_w - p_\infty}{\frac{1}{2} \rho_\infty V_\infty^2} \quad (5)$$

where p_w is the pressure acting on the body surface and p_∞ is the freestream pressure.

The pressure p_w on the body surface is calculated by the sum of the normal momentum fluxes of both incident and reflected molecules at each time step as follows,

$$p_w = p_i + p_r = \sum_{j=1}^N \{ [m_j v_{\eta j}^2]_{\downarrow} + [m_j v_{\eta j}^2]_{\uparrow} \} \quad (6)$$

where v_η is the component of the molecular velocity normal to the body surface.

Distribution of the pressure coefficient C_p along the lower and upper surfaces is demonstrated in Figures 7(a) and 7(b), respectively. According to this group of figures, it is seen that the pressure coefficient follows the same trend as that presented by the heat transfer coefficient in that it presents the maximum value at the stagnation region, decreases fast downstream along the upper body surface and increases downstream along the lower body surface. As indeed is clear from the Figure 7(a), changes on the upper surface shape caused the same effect on the pressure coefficient along the lower body surface, with the pressure coefficient distributions collapsing into one single curve.

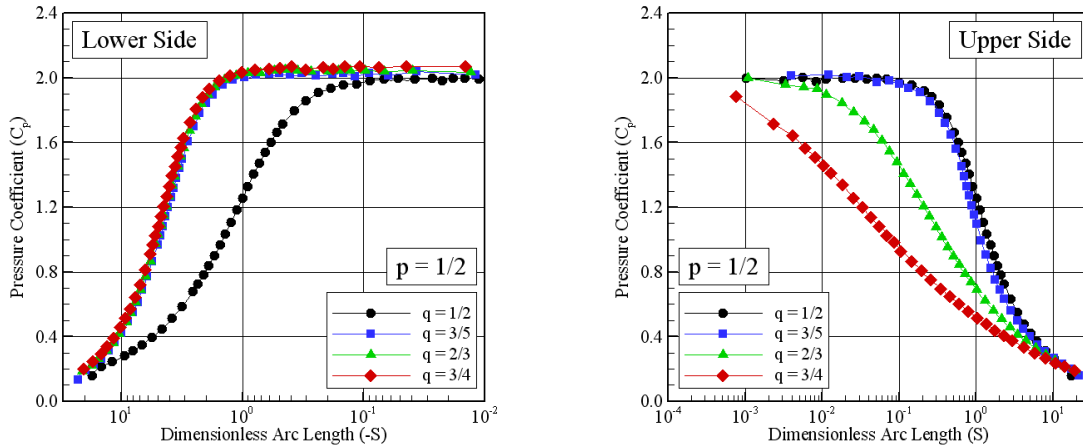


Figure 7: Distributions of the pressure coefficient C_p along the (a) lower and (b) upper surfaces as a function of the arc length S and parameterized by the power-law exponents.

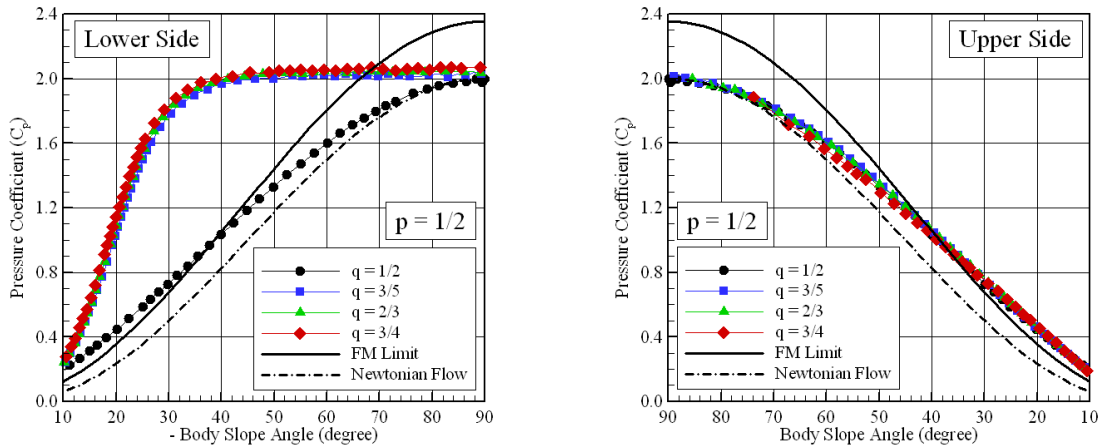


Figure 8: Distributions of the pressure coefficient C_p along the (a) lower and (b) upper surfaces as a function of the body slope angle and parameterized by the power-law exponents.

In the following, it proves helpful to explore the pressure coefficient C_p as a function of the body slope angle. In this manner, Figures 8(a) and 8(b) display the pressure coefficient C_p along the upper and lower surfaces, respectively. For comparative purpose, the pressure coefficient C_p obtained by assuming free molecular flow and Newtonian flow is also illustrated in this set of plots. It should be remarked that the Newtonian pressure coefficient is given by $2\sin^2\theta$, where θ is the body slope angle.

It is apparent from Figures 8(a) and 8(b) that the general shape of the pressure distribution profiles is preserved along the lower and upper surfaces when they are plotted as a function of the body slope angle.

6.4 Skin friction coefficient

The skin friction coefficient C_f is defined as being,

$$C_f = \frac{\tau_w}{\frac{1}{2}\rho_\infty V_\infty^2} \quad (7)$$

where τ_w is the shear stress acting on the body surface.

The shear stress τ_w on the body surface is calculated by the sum of the tangential momentum fluxes of both incident and reflected molecules at each time step. Nevertheless, for the diffuse reflection model imposed for the gas-surface interaction, reflected molecules have a tangential moment equal to zero, since the molecules essentially lose, on average, their tangential velocity component. As a result, the shear stress is given by the following equation,

$$\tau_w = \tau_i + \tau_r = \sum_{j=1}^N [m_j v_{\xi j}^2] \quad (8)$$

where v_{ξ} is the component of the molecular velocity tangent to the body surface.

The influence of the upper surface shape on the skin friction coefficient C_f is displayed in Figures 9(a) and 9(b) for the lower and upper surfaces, respectively. According to these plots, for the symmetric case of $p = q = 1/2$, the skin friction coefficient C_f starts from zero at the stagnation point, increases to a maximum value near the stagnation point and decreases downstream along the to body surface. By increasing the power-law exponent q from $1/2$ to $3/4$ on the upper surface shape, it is noticed that the skin friction coefficient presents roughly the same behavior than that observed for the symmetric case. It is noticed that the peak value increases and its location approaches the stagnation point, as shown in Figure 9(b). Nevertheless, for the lower surface, the peak value also increases but it moves far from the stagnation point when compared to that given by the symmetric leading edge. Of particular interest in the skin friction behavior is the negative values observed on the lower surface. It means that the shear stress direction is opposite to the flow direction.

The skin friction coefficient presents interesting features when it is displayed as a function of the body slope angle. Figures 10(a) and 10(b) shows these features for lower and upper surface, respectively. In these figures, a comparison with the skin friction coefficient by assuming a free molecular flow situation is also shown. As can be seen, the free molecular flow exhibits the maximum value for the skin friction coefficient at a station corresponding to 45 degrees. Similarly, the maximum values attained for the skin friction coefficient on the upper body surface, Figure 10(b), occur very close to the same station, i.e., 45 degrees. In contrast, for the lower body surface, Figure 10(a), the maximum values are displaced to a station around to 22 degrees. Therefore, it is noteworthy that changes on the upper surface shape affect the aerodynamic surface quantities on the lower surface.

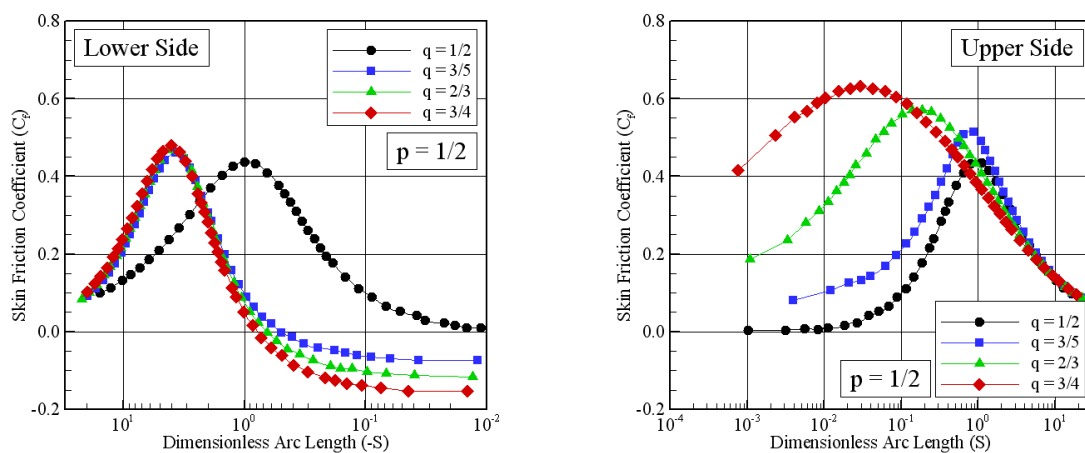


Figure 9: Distributions of the skin friction coefficient C_f along the (a) lower and (b) upper surfaces as a function of the arc length S and parameterized by the power-law exponents.

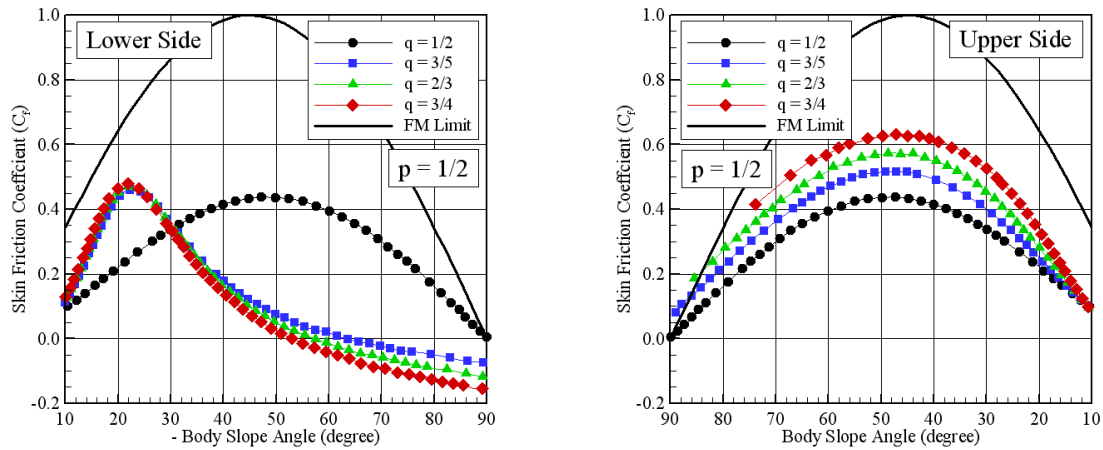


Figure 10: Distributions of the skin friction coefficient C_f along the (a) lower and (b) upper surfaces as a function of the body slope angle and parameterized by the power-law exponents.

6.5 Drag coefficient

The total drag coefficient C_d is defined as being,

$$C_d = \frac{F_D}{\frac{1}{2} \rho_\infty V_\infty^2 H} \quad (9)$$

where F_D is the resultant force acting on the body surface in the freestream direction and H is the height common to the leading edges, as shown in Figure 1(b).

The drag force on a surface in a gas flow results from the interchange of momentum between the surface and the molecules colliding with the surface. The total drag force is obtained by the integration of the pressure p_w and shear stress τ_w distributions along the lower and upper surfaces in the freestream direction. It is important to mention that the values for the total drag were obtained by assuming the shapes acting as leading edges. Therefore, no base pressure effects were taken into account on the calculations. Results for total drag are presented as total drag coefficient C_d and its components of pressure drag coefficient C_{pd} and the skin friction drag coefficient C_{fd} .

The leading-edge shape effect on total drag coefficient C_d is demonstrated in Figure 11 for the leading edges investigated. In this figure, the contributions of the pressure drag C_{pd} and the skin friction drag C_{fd} to the total drag C_d are compared to those for the symmetric leading edges investigated elsewhere (Santos and Lewis, 2002). In this fashion, filled symbols stand for the symmetric shapes, $p = q$, and the empty symbols for the asymmetric leading edges, $p = 1/2$ and $q = 3/5, 2/3, \text{ and } 3/4$.

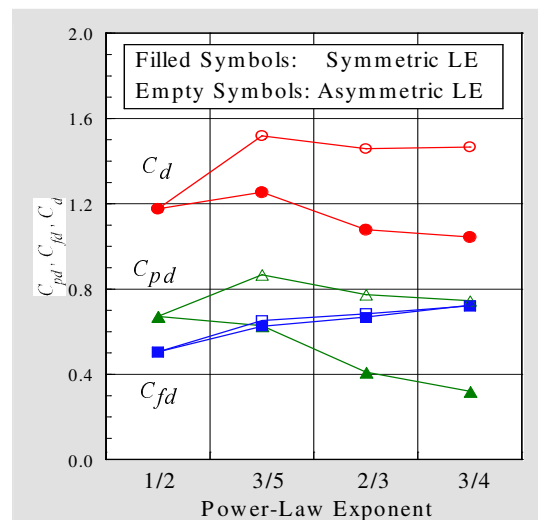


Figure 11: Pressure drag C_{pd} , skin friction drag C_{fd} and total drag C_d coefficients as a function of the power-law exponent.

Looking first at the drag results for the symmetric leading edges, it is seen that, for the p

= $q = 1/2$ case, the contribution of the pressure drag C_{pd} to the total drag is larger than that presented by the skin friction drag C_{fd} , a characteristic of a blunt body. In contrast, for the $p = q = 3/4$ case, the total drag coefficient C_d is dominated by the skin friction drag C_{fd} , a characteristic of a sharp body. As the net effect on total drag coefficient C_d depends on these two opposite behaviors, appreciable changes are observed in the total drag coefficient for the symmetric shapes, since C_{pd} and C_{fd} present different rates of changes. Nevertheless, the major contribution to the total drag coefficient C_d is attributed to the skin friction coefficient C_{fd} .

Turning next to the drag results for the asymmetric leading edges, it is observed that, as the power-law exponent q increases from $1/2$ to $3/4$, the contribution of the skin friction drag C_{fd} to the total drag coefficient C_d is pretty much the same as that presented by the corresponding symmetric leading edge. Conversely, the pressure contribution C_{pd} increases significantly. As a result, the total drag coefficient for hybrid power-law leading edges is enhanced as compared to that for symmetric power-law leading edges.

6.6 Lift coefficient

The total lift coefficient C_l is defined as being,

$$C_l = \frac{F_L}{\frac{1}{2} \rho_\infty V_\infty^2 H} \quad (10)$$

where F_L is the resultant force acting on the body surface perpendicular to the freestream direction and H is the height common to the leading edges, as shown in Figure 1(b).

The lift force on a surface in a gas flow results from the interchange of momentum between the surface and the molecules colliding with the surface. The total lift force is obtained by the integration of the pressure p_w and shear stress τ_w distributions along the lower and upper surfaces perpendicular to the freestream direction. Similar to the drag coefficient, results for total lift are presented as total lift coefficient C_l and its components of pressure lift coefficient C_{pl} and the skin friction lift coefficient C_{fl} .

The extent of changes on total lift coefficient C_l due to variations on the upper surface shape is illustrated in Figure 12 as a function of the power-law exponent.

According to Figure 12, it is noticed that the total lift C_l presents an expressive rise with increasing the power-law exponent dictated by the contribution of the pressure lift C_{pl} . In contrast, the contribution of the skin friction C_{fl} is in the sense of reducing the total lift C_l .

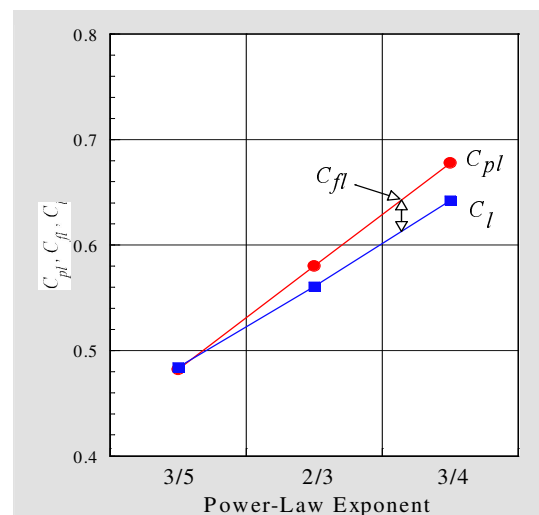


Figure 12: Pressure lift C_{pl} , skin friction lift C_{fl} and total lift C_l coefficients as a function of the power-law exponent.

7. CONCLUDING REMARKS

This study presented a detailed analysis of the aerodynamic surface quantities on power-law leading edges in rarefied hypersonic flow by employing the DSMC method. The calculations provided information concerning the nature of the number flux, heat transfer, pressure, skin friction, drag and lift coefficients for a family of contours composed by lower

and upper surface with different power-law exponents. The emphasis of the investigation was to compare symmetric power-law leading edges with asymmetric power-law leading edges in order to determine which geometry is better suited as a blunting profile for hypersonic configurations.

It was found that hybrid power-law leading edges presented lower stagnation point heating than their corresponding symmetric power-law leading edges. The analysis also indicated that the total drag for hybrid power-law leading edges was larger than that for symmetric power-law leading edges.

It is apparent that each comparison resulted in a different conclusion for which geometry performs better. Thus, the ideal blunt leading edge relies on the context. If stagnation point heating is the primary issue in leading-edge design of hypersonic waveriders, then hybrid power-law leading edges are superior to their corresponding symmetric power-law leading edges. However, in order to assess the overall performance of hybrid power-law leading edges, it becomes imperative to investigate the shock-wave standoff distance, since waveriders depend on leading-edge shock attachment in order to achieve their high lift-to-drag ratio at high lift coefficient. Nevertheless, the investigation of the shock-wave structure on these new shapes is the subject for future work.

8. REFERENCES

- Alexander, F. J., Garcia, A. L., and, Alder, B. J., 1998, Cell size dependence of transport coefficient in stochastic particle algorithms. *Physics of Fluids*, vol. 10, n. 6, pp. 1540-1542.
- Alexander, F. J., Garcia, A. L., and, Alder, B. J., 2000, Erratum: Cell size dependence of transport coefficient is stochastic particle algorithms. *Physics of Fluids*, vol. 12, n. 3, pp. 731-731.
- Bird, G. A., 1981, Monte Carlo simulation in an engineering context. In Fisher, S. S., ed, *Progress in Astronautics and Aeronautics: Rarefied gas Dynamics*, vol. 74, part I, AIAA New York, pp. 239-255.
- Bird, G. A., 1989, Perception of numerical method in rarefied gasdynamics. In Muntz, E. P., Weaver, D. P. & Capbell, D. H., eds, *Rarefied gas Dynamics: Theoretical and Computational Techniques*, vol. 118, AIAA, New York, pp. 374-395.
- Bird, G. A., 1994, *Molecular Gas Dynamics and the Direct Simulation of Gas Flows*, Oxford University Press, Oxford, England, UK.
- Mason, W. H. and Lee, J., 1994, Aerodynamically blunt and sharp bodies. *Journal of Spacecraft and Rockets*, vol. 31, n. 3, pp. 378-382.
- Nonweiler, T. R. F., 1959, Aerodynamic problems of manned space vehicles, *Journal of the Royal Aeronautical Society*, vol. 63, Sept, pp. 521-528.
- Santos, W. F. N., and Lewis, M. J., 2002, Power-law shaped leading edges in rarefied hypersonic flow. *Journal of Spacecraft and Rockets*, vol. 39, n. 6, pp. 917-925.
- Santos, W. F. N., and Lewis, M. J., 2005a, Calculation of shock wave structure over power-law bodies in hypersonic flow. *Journal of Spacecraft and Rockets*, vol. 42, n. 2, pp. 213-222.
- Santos, W. F. N., and Lewis, M. J., 2005b, Aerothermodynamic performance analysis of hypersonic flow on power-law leading edges. *Journal of Spacecraft and Rockets*, vol. 42, n. 4, pp. 588-597.
- Santos, W. F. N., 2005, "Leading-edge bluntness effects on aerodynamic heating and drag of power law body in low-density hypersonic flow. *Journal of the Society of Mechanical Sciences and Engineering*, vol. 27, n. 3, pp. 236-241.
- Santos, W. F. N., 2008, Physical and computational aspects of shock waves over power-law leading edges. *Physics of Fluids*, vol. 20, n. 1, pp. 1070631-11.